Supplemental material for multivalent optical cycling centers: towards control of polyatomics with multi-electron degrees of freedom

Phelan Yu,[1,*] Adrian Lopez,[1] William A. Goddard III,[2,3] and Nicholas R. Hutzler[1]

[1] *Division of Physics, Mathematics, and Astronomy, California Institute of Technology, Pasadena, California 91125, USA*
[2] *Materials and Process Simulation Center, California Institute of Technology, Pasadena, California 91125, USA*
[3] *Division of Chemistry and Chemical Engineering, California Institute of Technology, Pasadena, California 91125, USA*

(Dated: November 6, 2022)

Appendix A: Details on vibronic structure

1. Molecular orbital configurations

The electronic structures of the MSH multivalent systems considered in this manuscript follow a common molecular orbital (MO) pattern. This can be seen by correlating the $3s$ and $3p$ shells of the cycling center (i.e. Al, Si, and P-like) to the valence orbitals of the hydrosulfide ligand (-SH), which are the S-H σ-bonding, S($3p\sigma$) unpaired electron, and S($3p\pi$) lone pair orbitals. This forms an MO progression that, in order of increasing energy, can be described as S-H σ-bonding ($1a'$), M-S σ-bonding ($2a'$), M-S π-bonding ($1a''$), M-S σ-antibonding ($1a'^*$), S-H σ-antibonding ($2a'^*$), and M-S π-antibonding ($1a''^*$) orbitals, as depicted in Fig. 1, reproduced here from the main text. A fourth non-bonding orbital ($3a'^*$) is formed from M($3d\sigma$)-localized orbitals. These orbitals partially correlate to the ligand S($3p\sigma$) orbital and also mix into the M-S σ bonding orbital, as indicated by the dotted line maps in the figure. Higher angular momentum orbitals out of the M(d)-shell are not implicated in our analysis of photon cycling channels and therefore not examined for the sake of brevity.

For each model multivalent molecule (i.e. AlSH, SiSH, PSH), we perform natural transition orbital (NTO) analyses to elucidate the nature of the EOM-CC transitions calculated in this work. Hole-orbital isosurfaces (iso = 0.05) and amplitudes ($\bar{\sigma}$) for dominant NTO components are plotted in the upper panels of Fig. 1 and numbered from (i) up to (vi), which correspond to unique EOM-CC transitions for each molecule. The EOM-CC calculations are performed as described in the main text: AlSH using EOM-EE-CCSD with a singlet ground state reference, SiSH using EOM-SF-CCSD with a quartet excited state reference, and PSH using EOM-EE-CCSD with a singlet excited state reference. Curved lines with arrows overlaid on the MO schematics in Fig. 1 depict the primary MO configurations involved in the NTO components for each transition.

As discussed in Sec. 3 of the main text, the highest occupied molecular orbital of the AlSH ground manifold corresponds to two paired electrons occupying the Al($s\sigma$) orbital or $1a'^*$, which is the M-S σ-antibonding orbital. Excited state triplet progressions, as depicted by the natural transition orbital analysis in Fig. 1(a), correspond to spin-forbidden excitations out of $1a'^*$ into the higher lying in-plane Al($3p$) or $2a'^*$ orbital [i: $\tilde{X}^1A' \rightarrow \tilde{a}^3A'$], which maps to the intermediate decay state, the out-of-plane Al($3p$) or $1a''^*$ orbital [ii: $\tilde{X}^1A' \rightarrow \tilde{b}^3A''$], which is the cycling line, and the in-plane Al($3d\sigma$) or $3a'^*$ orbital [iii: $\tilde{X}^1A' \rightarrow \tilde{c}^3A'$].

The ground singlet-to-excited singlet transitions are described by a similar progression, with the first two transitions corresponding to spin-preserving excitations from $1a'^*$ into the $2a'^*$ [iv: $\tilde{X}^1A' \rightarrow \tilde{A}^1A'$] and $1a''^*$ orbitals [v: $\tilde{X}^1A' \rightarrow \tilde{B}^1A''$]. The third singlet-to-singlet transition [vi: $\tilde{X}^1A' \rightarrow \tilde{C}^1A'$] has mixed character, with NTO transitions from both the Al($s\sigma$) localized hole ($1a'^*$) exciting to a particle orbital with Al($d\sigma$) and S-H antibonding components [vi.1] – which we approximately describe as $3a'^*$ – as well as excitations from the subvalent Al-S π-bonding orbital ($1A''$) into the Al-S π-antibonding orbital ($1a''^*$) [vi.2]. The significant lengthing of the Al-S bond from upon excitation to both the $\tilde{c}^3A'$ and $\tilde{C}^1A'$ states confirms the charge-transfer nature of the NTO excitations to a delocalized Si($d\sigma$) orbital as depicted by [iii] and [vi.1].

For SiSH, the highest occupied molecular orbital (HOMO) corresponds to a single unpaired electron localized on the in-plane Si($3p\pi$) orbital ($2a'^*$). Excitations to the two lowest lying quartet states correspond to spin-forbidden transitions [i: $\tilde{X}^2A' \rightarrow \tilde{a}^4A''$] between the antibonding $1a'^*$ to the M-S π-antibonding orbital ($1a''^*$) and the M-S π-bonding orbital to the M-S π antibonding orbital [ii: $\tilde{X}^2A' \rightarrow \tilde{b}^4A'$]. The proposed photon cycling channel for SiSH is between the ground and first excited quartet state, which have similar equilibrium geometries. Spin-allowed doublet-doublet excitations, meanwhile, correspond to transitions between the Si($3p\pi$)-localized $2a'^*$ orbitals to the M-S π-antibonding orbital ($1a''^*$) [iii: $\tilde{X}^2A' \rightarrow \tilde{A}^2A''$] and transitions between the Si($3s\sigma$) antibonding orbital ($1a'^*$) and the in-plane σ-antibonding orbital [iv: $\tilde{X}^2A' \rightarrow \tilde{B}^2A'$]. The third doublet-doublet transition [v: $\tilde{X}^2A' \rightarrow \tilde{C}^2A'$] has highly mixed character, which we approximately describe as excitations out of the in-plane Si($p\pi$) antibonding or-

* phelanyu@caltech.edu

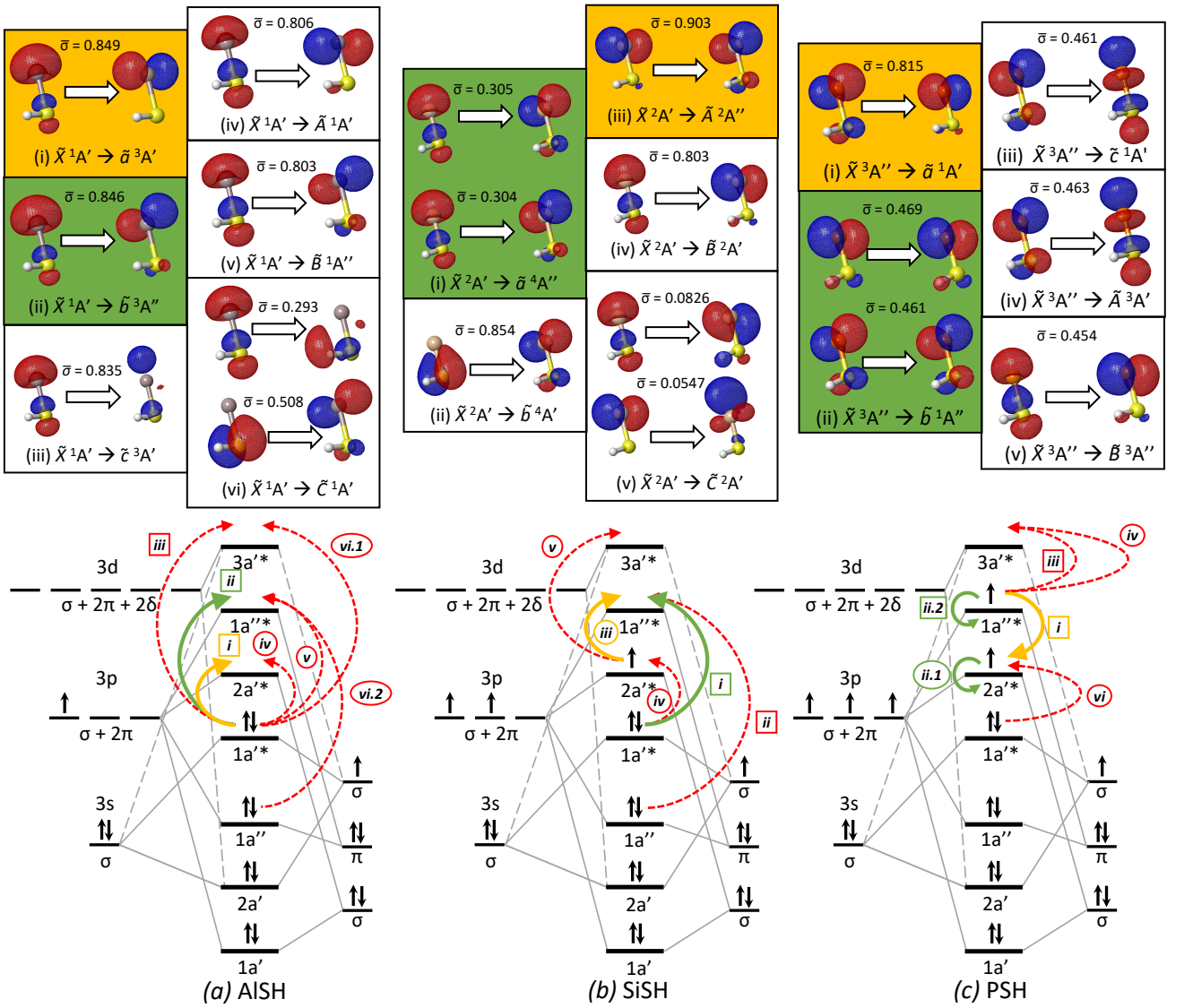

Figure 1. Natural transition orbitals (isovalue = 0.05) for low-lying electronic transitions (top) and molecular orbital correlation diagrams (bottom) of three model multivalent species: (a) AlSH, (b) SiSH, and (c) PSH, as reproduced from fig. 6 in the main text. Within each NTO panel are particle-hole pairs for the labeled transition, where $\bar{\sigma}$ denotes the relative NTO amplitude of each pair. Highlighted in green and yellow panels are the primary cycling and ground-to-intermediate state transitions, following the convention of table 1 in the main text in the main text. NTO calculations are performed using (a) EOM-EE-CCSD with a singlet ground state reference, (b) EOM-SF-CCSD with a quartet excited state reference, (c) and EOM-EE-CCSD with a singlet excited state reference. Below the NTO diagrams are MO correlation diagrams, which – for each of the three molecules – depict the ground state MO and spin configurations that are formed from the correlation of cycling center (left) and hydrosulfide ligand (right) orbitals. Each MO is labeled by its C_s symmetry character (A', A''), whereas the symmetry content of atomic and diatomic ligand orbital shells are labeled by $C_{\infty v}$ representations (σ, π, δ...), which are described in the text. Curved arrows correspond to hole-particle NTO transitions depicted in the upper panels, which are individually identified by roman numerals, with subdivisions for transitions with multiple significant NTO components. Transitions labels surrounded by circles and squares indicate spin-allowed and spin-forbidden transitions, respectively. The cycling and ground-to-intermediate state transitions are identified with green and yellow solid arrows, following the earlier color convention, while the remaining transitions are identified with dashed red arrows.

bital ($2a'^*$) into the Si($d\sigma$) antibonding orbital ($3a'^*$).

As discussed earlier, PSH has a high-spin triplet ground state due to spin exchange and nodal plane effects. In the MO schematic, this configuration corresponds to two unpaired spins distributed between the in-plane ($2a'^*$) and out-of-plane ($1a''^*$) Si($3p\pi$)-localized antibonding orbitals. The first spin-forbidden transition [i: $\tilde{X}^3A'' \rightarrow \tilde{a}^1A'$] the intermediate singlet state corresponds to a spin-forbidden from the upper Si($3p\pi$)-localized $1a''^*$ orbital to the lower $2a'^*$ orbital. This is a

higher energy configuration due to the nodal separation between the two Si($p\pi$) lobes and the spin exchange energy, which is positive for paired electrons occupying the $2a'^*$ orbital. The cycling transition to the second singlet state [ii: $\tilde{X}^3A'' \rightarrow \tilde{b}^1A''$], corresponds to a spin-forbidden within the upper $1a''^*$ orbital [ii.2], as indicated by the opposite phase convention in the hole-particle isosurfaces. A trivial $2a'^* \rightarrow 2a'^*$ transition component [ii.1] is also identified by the NTO analysis, which we depict in Fig. 1 for completeness. The third spin-forbidden transition [iii: $\tilde{X}^3A'' \rightarrow \tilde{c}^1A'$] corresponds to spin-forbidden excitations from the unpaired Si(3π)-localized $1a''^*$ antibonding orbital to the Si($3d\sigma$)-localized $3a'^*$ antibonding orbital.

The spin-preserving triplet-to-triplet transitions, meanwhile correspond to excitations from the frontier $1a''^*$ antibonding orbital to the Si($3d\sigma$)-localized $3a'^*$ antibonding orbital [iv: $\tilde{X}^3A'' \rightarrow \tilde{A}^3A'$] and excitation of a single electron from the sub-valence Si($3s\sigma$)-localized $1a'^*$ antibonding orbital to pair to the unpaired electron in the lower Si($3p\pi$)-localized $2a'^*$ orbital [v: $\tilde{X}^3A'' \rightarrow \tilde{B}^3A''$].

2. Valence bonding and repulsion

As discussed in Sec. 4(a), the interplay of bonding, ionicity, and repulsion in MSH multivalent species plays an important role in determining the ground and excited state geometries, and by extension, the vibronic branching and viable photon cycling pathways. Bonding and repulsion are largely described by interactions between localized electron orbitals of the constituent atoms. The delocalized nature of the MO basis considered in the previous section therefore makes it unsuitable for visualizing these effects.

To examine the localized nature of bonding and lone pair orbitals depicted schematically in Fig. 4 of the main text, we generate generalized valence bond (GVB) natural orbitals [1, 2] from canonical MOs using a Sano-type procedure [3] for each of the multivalent classes. The Pipek-Mezey (PM) scheme [4] is used to compute localized molecular orbitals that initialize the method, and all calculations are peformed over CCSD/aug-cc-pVTZ-optimized geometries. Fig. 2 depicts the localized GVB natural orbitals for representative systems from each of the three multivalent classes (AlSH, PSH, SiSH), as well as accompanying GVB diagrams. Plots and diagrams of valence bonding and non-bonding orbitals are labeled as ϕ_i using the index $i = 1, .., 5$.

In the case of AlSH (see Fig. 6(a) of the main text), ϕ_1 denotes the paired Al-centered $3s\sigma$ orbital, which is the frontier GVB natural orbital and approximately describes the paired Al-centered cycling electrons. For the SiSH molecule (see Fig. 6(b) of the main text), ϕ_1 denotes the non-bonding Si-centered in-plane $3p\pi$ orbitals, which approximately describes the single unpaired Si-centered cycling electron. For the PSH molecule (see Fig. 6(c) of the main text), $\phi_{1'}$ and $\phi_{1''}$ denote the unpaired

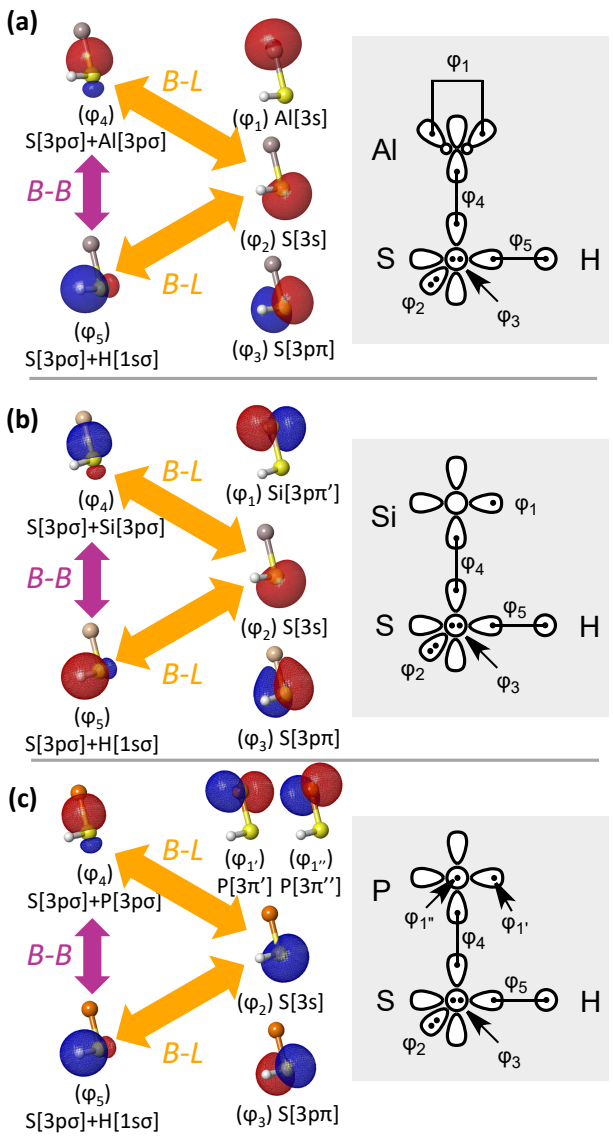

Figure 2. Generalized valence bond (GVB) natural orbitals and diagrams for molecules representative of the three multivalent classes: (a) AlSH, (b) SiSH, and (c) PSH. Depicted on the left side of each sub-panel are the five highest occupied bonding and non-bonding GVB natural orbitals (iso = 0.05), labeled ϕ_1 to ϕ_5 and by their main atomic orbital contributions. Details of the procedure used to generate the orbitals are described in Appendix A(2). The colored arrows $B - B$ (purple) and $B - L$ (yellow) indicate bond-bond and bond-lone pair repulsion between the plotted orbitals. The right inset of each sub-panel (gray background) contains the corresponding GVB diagram.

in and out-of-plane $3p\pi$ orbitals that approximately describe the triplet unpaired P-centered cycling electrons.

The remaining four GVB natural orbitals have common descriptions among all three molecules. ϕ_2 and ϕ_3 refer to in-plane s and out-of-plane $p\pi$ lone pairs that are centered on the S atom, respectively. ϕ_4 and ϕ_5, meanwhile, refer to the metal-S and S-H bonding orbitals, re-

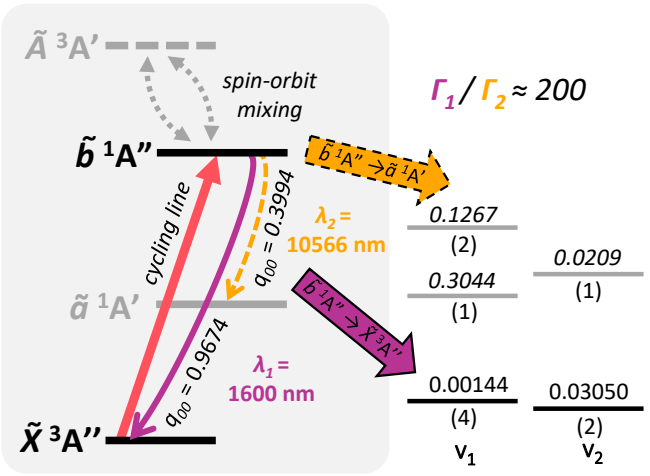

Figure 3. Optical cycling schemes for group 15 systems, demonstrated using BiSH vibrational branching ratios. The main excitation transition (red solid arrow) is from $\tilde{X}^3A''$ to $\tilde{b}^1A''$. On the left, solid curved (purple) and dashed curved (yellow) lines denote vibration-free decays to vibrational channels in the $\tilde{X}^3A''$ and $\tilde{a}^1A'$ manifolds, respectively, after spontaneous emission from the $\tilde{b}^1A''$ upper state. Pairs of gray dashed arrows depict the spin-orbit induced mixing between the first excited singlet state $\tilde{A}^3A'$ and the upper $\tilde{b}^1A''$ state. Levels on the right hand side depict leading off-diagonal FCFs for decays to the $\tilde{a}^1A'$ and $\tilde{X}^3A''$ manifolds, with corresponding transition wavelengths denoted λ_2 and λ_1, respectively. Decimals above the levels denote the Franck-Condon factors (eq. 1 in the main text) normalized relative to the respective electronic transition, while numbers underneath indicate the vibrational quanta in each mode (v_i). Due to spin-orbit effects from the Bi center, more than 99.5% of decays out of the $\tilde{b}^1A''$ state connect directly to the $\tilde{X}^3A''$ state, as indicated by the suppression factor (Γ_1/Γ_2) in the upper right hand corner (see Table 1 in the main text). Analogous pathways can be utilized to construct cycling schemes for other group 15 species, and branching patterns for other multivalent classes can be found in the Fig. 5 in the main text and Fig. 4 in the appendix. Level spacings are not drawn to scale.

spectively. As discussed in Sec. 3 and 4 of the main text, the bond angle of the molecule is determined by competition between the effects of bond-bond repulsion and lone pair-bond repulsion. Consistent with the notation in Fig. 4 of the main text, the labeled arrow $B-B$ (green) in Fig. 2 depicts the repulsive interaction between the metal-S (ϕ_4) and S-H (ϕ_5) bonding orbitals, while the $B-L$ arrows (yellow) depict the repulsion between the S in-plane lone pair (ϕ_2) and the bonding orbitals (ϕ_4) and (ϕ_5).

3. Vibrational Closure Schemes

In this section, we elaborate on the details of the optical cycling schemes for each class of multivalent molecules, as initially discussed in the main text in Sec. 1, and depicted in Fig. 5 for a model group 13 molecule, namely AlSH. Additional photon cycling and vibrational closure schemes – for group 15 and 14 molecules – shown here in Fig. 3 and 4, respectively. Both figures depict the main cycling line (red arrows) between the ground state and spin-forbidden out-of-plane upper state, as well as dominant vibrational decays to off-diagonal vibrationals in the ground and intermediate electronic manifolds.

In the case of class 15 molecules (Fig. 3), the ground state is a high-spin $\tilde{X}^3A''$ manifold, while the upper cycling state is a $\tilde{b}^1A''$ singlet state. This transition is allowed by spin-orbit induced intensity borrowing on dipole-allowed $\tilde{X}^3A'' \rightarrow \tilde{A}^3A'$ channel. Dominant off-diagonal vibrational decays to both the ground and intermediate $\tilde{a}^1A'$ state are illustrated in blue and yellow (dotted boundary) panels, respectively. While the scheme here specifically utilizes FC data for BiSH (which has high electronic branching into the ground state), the photon cycling scheme depicted here is generally applicable to other group 15 systems listed in Table 1 in the main text of the main text.

Meanwhile, Fig. 4 illustrates cycling and vibrational closure schemes for group 14 molecules, utilizing SiSH as a model system. Here, the ground state is a $\tilde{X}^2A'$ manifold, with a quasi-diagonal cycling transition to the upper $\tilde{a}^4A''$ state. This transition is allowed both by a combination of spin-orbit intensity borrowing from the $\tilde{X}^2A' \rightarrow \tilde{B}^2A'$ transition, as well as direct mixing of $\tilde{a}^4A''$ with the opposite-symmetry ground state. Leading vibrational decays to the ground and intermediate ($\tilde{A}^2A''$) are again depicted with an analogous color scheme to the figures for group 13 and 15 molecules. Note that although the vibrationless FCF of the intermediate $\tilde{a}^4A'' \rightarrow \tilde{A}^2A''$ decay can be comparable, or sometimes even higher than the primary $\tilde{a}^4A'' \rightarrow \tilde{X}^2A''$ line, it is not preferred as an optical cycling channel due to the relatively weak intensity of these transitions, as indicated in Table 1 of the main text, as well as the existence of rapid decays into the ground state from $\tilde{A}^2A''$ via relatively non-diagonal vibronic channels.

4. Alternative ligands

As discussed in the introduction and Sec. 3 of the main text, traditional approaches to constructing laser coolable molecules by bonding cycling centers to highly electronegative ligands appear to fail for multivalent OCCs. This is evident from poor Franck-Condon performance for a variety of multivalent species built from aluminum centers bonded to common pseudohalogen ligands, including hydroxide (-OH), (iso)cynanide (-CN), cyanate (-NCO), acetylide (-CCH), fluoroacetylide (-CCF), and the superhalogen boron dioxide (-OBO).

Data for these alternative systems, including low lying singlet and triplet Franck-Condon factors, Mulliken charge differences between metal and linker atoms, as

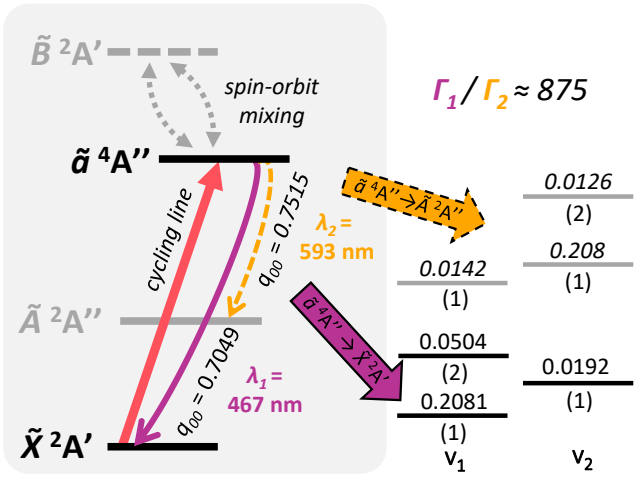

Figure 4. Optical cycling schemes for group 14 systems, demonstrated using SiSH branching ratios. The main excitation transition (red solid arrow) is from $\tilde{X}^2A'$ to $\tilde{a}^4A''$. On the left, solid curved (purple) and dashed curved (yellow) lines denote vibration-free decays to vibrational channels in the $\tilde{X}^2A'$ and $\tilde{A}^2A''$ manifolds, respectively, after spontaneous emission from the $\tilde{a}^4A''$ upper state. Pairs of gray dashed arrows depict the spin-orbit induced mixing between the first excited singlet state $\tilde{B}^2A'$ and the upper $\tilde{a}^4A''$ state. Levels on the right hand side depict leading off-diagonal FCFs for decays to the $\tilde{A}^2A''$ and $\tilde{X}^2A'$ manifolds, with corresponding transition wavelengths denoted λ_2 and λ_1, respectively. Decimals above the levels denote the Franck-Condon factors (eq. 1 in the main text) normalized relative to the respective electronic transition, while numbers underneath indicate the vibrational quanta in each mode (v_i). Due to spin-orbit effects from the Si center, more than 99.88% of decays out of the $\tilde{a}^4A''$ state connect directly to the $\tilde{X}^2A'$ state, as indicated by the suppression factor (Γ_1/Γ_2) in the upper right hand corner (see Table 1 in the main text). Analogous pathways can be utilized to construct cycling schemes for other group 14 species, and branching patterns for other multivalent classes can be found in the Fig. 5 in the main text and Fig. 3 in the appendix. Level spacings are not drawn to scale.

well as calculated and experimental ligand electron affinities can be found in Table I. All geometry, frequency, and charge density calculations are performed in line with methods described in the main text, using the EOM-EE-CCSD method and basis sets of aug-cc-pVTZ quality. Ligand electron affinity is calculated from the energy difference between an anion reference and a neutral configuration, with geometries optimized using CCSD and EOM-IP-CCSD, respectively.

Unlike aluminum hydroxide (AlOH), which adopts a bent geometry in the ground state, as described earlier, the additional pseudohalogen ligands we consider in this section and Table I bond to Al to form molecules that are predicted to have linear ground states, due to either (1) the use of an non-chalcogen linker atom (e.g. C, N) and therefore absence of lone-pair repulsive effects or (2) highly electronegative metal-ligand interactions that overcome lone-pair repulsive effects (e.g. AlOBO). Despite the apparent stability of their linear ground state configurations, all of these molecules also possess excited state geometries that are calculated to have either (1) significantly different metal-ligand bond lengths relative to the ground state and/or (2) large metal-ligand bend. Either of these properties leads to large off-diagonal FC behavior, which is fatal to achieving vibrationally closed photon cycling.

The precise nature of the bonding mechanisms that produce low vibrationless FCFs in the molecules (and transitions) considered here is non-generic and highly species-dependent. In addition, the set of alternative pseudohalogen ligands considered here – while representative of molecules previously analyzed in the laser-cooling literature – is non-exhaustive. We are nonetheless able to extract some useful observations.

First, there is no global correlation between bond ionicity, measured both in terms of ligand electron affinity and Mulliken charge difference between the linker and cycling atom, and Franck-Condon behavior, although slight improvements can be observed by switching to a more ionic isomer (e.g. AlCN vs. AlNC). Second, oxygen-containing ligands tend to perform poorly with multivalent cycling centers, regardless of ligand electronegativity. This is due to the interaction of the oxygen lone pair with high orbital angular momentum ($\Lambda > 0$) electrons centered on the Al metal. This is most easily seen with AlOH, as discussed earlier, but is also observed in AlNCO and AlOBO, where excitation from a linear Al($3s\sigma$)-like ground state into Al($3p\pi$)-like excited manifolds leads to bond angle bending and breaking of the linear symmetry due to interactions between the Al($3p\pi$) orbitals and oxygen lone pairs. Third, despite the low performance of FCFs considered in Table I, spin-forbidden (triplet) transitions from the ground state do appear, for molecules considered, to perturb molecular geometries less relative to dipole-allowed singlet channels, which is consistent with earlier findings for AlSH.

Appendix B: Details on rotational structure and closure

Repumping of rotational decays in bent molecules can be achieved by addressing sidebands that are allowed by rotational and parity selection rules [11]. As discussed earlier, the broken symmetry of ATMs complicates the rotational level structure, which is described by the rigid rotor Hamiltonian

$$H_{\text{rot}} = A\mathbf{N}_a^2 + B\mathbf{N}_b^2 + C\mathbf{N}_c^2, \tag{B1}$$

where we have three unique rotational constants ($A = \hbar/I_a 4\pi$, $B = \hbar/I_b 4\pi$, $C = \hbar/I_c 4\pi$) and three spinless angular momentum operators $\mathbf{N}_i$ along the i-axis (see Fig. 3 of the main text for axis convention). The rigid rotor spectrum described by H_{rot} is labeled by the term N_{K_a,K_c}. Here, N is the total angular momentum without

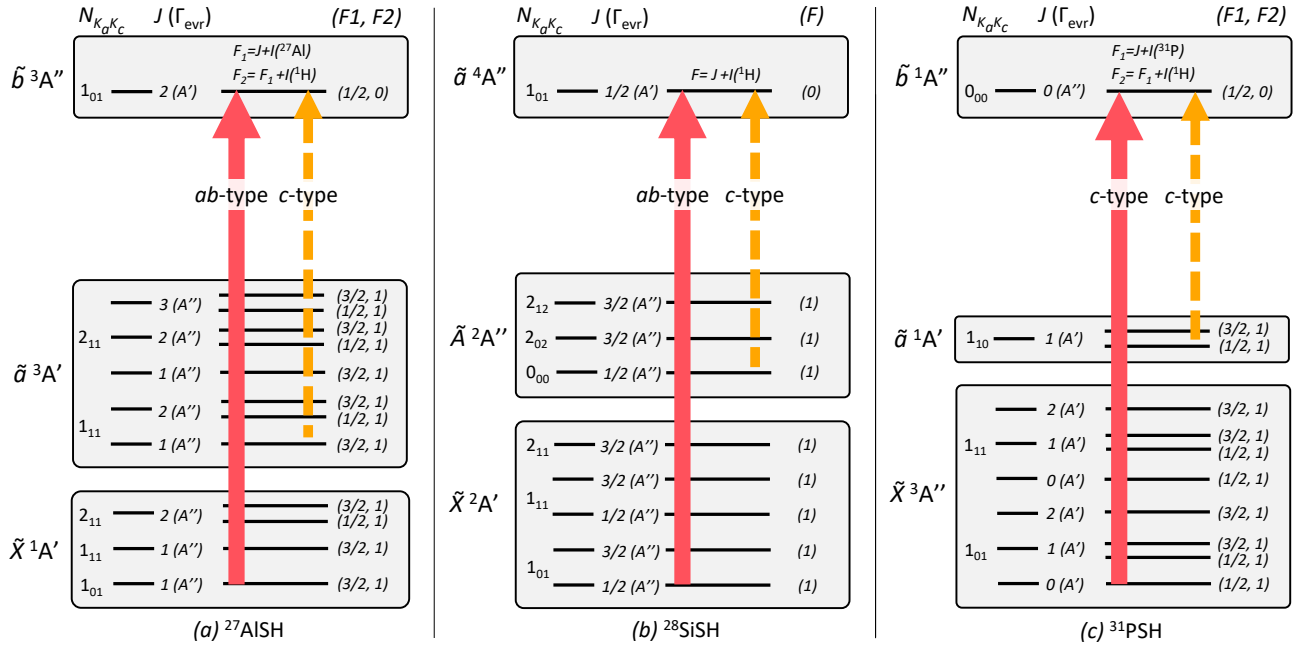

Figure 5. Proposed rotational repumping scheme based on optical transitions identified for (a) ^{27}AlSH, (b) ^{28}SiSH, and (c) ^{31}PSH in Fig. 5. Levels are listed using N_{K_a,K_c}, J, and F_i quantum numbers. In molecules with both metal $I(^Z\mathrm{M})$ and hydrogen spins $I(^1\mathrm{H})$, $F_1 = J + I(^Z\mathrm{M})$ and $F_2 = F_1 + I(^1\mathrm{H})$ denote the metal (M) and total hyperfine numbers, respectively, where Z is the atomic mass of the metal. In open-shell states, the rotational levels are split by spin-orbit ($\mathbf{\Lambda_a}\cdot\mathbf{S}$) and spin-rotation ($\mathbf{N}\cdot\mathbf{S}$) couplings. For each spin-rotation branch, $\Gamma_{\rm evr}$ denotes the combined rovibronic-spin symmetry $\Gamma_{\rm el}\times\Gamma_{\rm vib}\times\Gamma_{\rm rot}$ of the level. The red, thick solid line denotes the primary $F \to F-1$ cycling transition from the ground state to the out-of-plane target state. The yellow, thin dashed lines denote rotationally closed repumps out of the intermediate manifold. Note that for spin-forbidden transition, only parity selection rules (see Table III) are applied, while for spin-allowed transitions, both angular momentum rules (see Table II) and parity are applied.

Molecule	(a) $\tilde{A} \to \tilde{X}$	(b) $\tilde{a} \to \tilde{X}$	$\Delta Q_{\rm IAO}$	EA (calc/exp)
AlCCH	0.2533	0.4852	0.8630	3.102/2.969(6)[5]
AlCCF	< 0.01	0.48021	0.9804	3.383/$\gtrsim$ 3.4(8)[6]
AlNCO	–	< 0.01	1.229	3.652/3.609(5)[7]
AlCN	0.1598	0.3177	0.7344	3.989/3.862(4)[7]
AlNC	0.4734	0.6417	1.060	3.989/3.862(4)[7]
AlOBO	–	–	1.387	4.465/4.46(3)[8]

Molecule	(c) $\tilde{B} \to \tilde{X}$	(d) $\tilde{b} \to \tilde{X}$	$\Delta Q_{\rm IAO}$	EA (calc/exp)
AlSH	0.2030	0.9974	0.7963	2.322/2.317(2)[9]
AlOH	0.0509	0.2468	1.456	1.761/1.82765(25)[10]

Table I. Vibrationless Franck-Condon factors (q_{00}) for electronic transitions labeled (a)-(d), IAO charge difference (a.u.) across the metal ligand bond ($Q_{\rm IAO}$), and ligand electron affinity (eV) for (top) linear (Σ^+) ground state and (bottom) bent (A') ground state molecules. In order of appearance, the full term symbols for the transitions considered in the tables are: (a) $\tilde{A}^1\Pi \to \tilde{X}^1\Sigma^+$, (b) $\tilde{a}^3\Pi \to \tilde{X}^1\Sigma^+$, (c) $\tilde{B}^1A'' \to \tilde{X}^1A'$, and (d) $\tilde{b}^3A'' \to \tilde{X}^1A'$. For the upper table, FCFs labeled by an asterisk indicate transitions between a nonlinear or quasi-linear excited state and the linear ground state. Entries with "–" indicate excited states that converge on strongly bent transition states due to the interaction of the Al($3p\pi$) orbital with the oxygen lone pair.

electron (S) and nuclear spin (I), while K_a and K_c are approximate quantum numbers that correspond to the projection of N onto the symmetry axis of the molecule if it were distorted to the limit of becoming a prolate (a-axis, $A > C$) or oblate (c-axis, $C > A$) symmetric top, respectively. Couplings to electronic and nuclear spins introduce the angular momenta $J = N + S$ and $F = J + I$. These quantum numbers encapsulate the level shifts induced by spin-orbit and hyperfine effects in the molecule.

Table II. Symmetries of N_{K_a,K_b} rotational wavefunctions for prolate ATMs in terms of irreps of C_{2v} and C_s point groups, classified by the signs (σ) of K_a and K_c. Parity selection rules for dipole transitions arise from the requirement $\Gamma_1\times\Gamma_2 \subset \Gamma^*$, where $\{\Gamma_1, \Gamma_2\}$ are the symmetries of two rovibronic states and Γ^* is the electric dipole representation [12].

$\sigma(K_a)$	$\sigma(K_c)$	$\Gamma_{\rm rot}(C_{2v})$	$\Gamma_{\rm rot}(C_s)$
+1	+1	A_1	A'
+1	−1	A_2	A''
−1	−1	B_1	A''
−1	+1	B_2	A'

Each rotational state also has a symmetry classification ($\Gamma_{\rm rot}$) in terms of the irreducible representations of the

Table III. Approximate angular momentum selection rules for dipole-allowed transitions in asymmetric top molecules, as adapted from [11]. These rules occur in addition to the standard rules on total angular momentum $\Delta J = 0, \pm 1$ and $J' \nleftrightarrow J'' = 0$, as well as the constraint that $K_a + K_c = N$ or $N+1$ for $0 \leq K_{a,c} \leq N$.

$\hat{\mu}$-axis	ΔK_a	ΔK_c	Special cases
a-type	0	± 1	$\Delta N \neq 0$ for $K_a' \to K_a'' = 0$
b-type	± 1	± 1	
c-type	± 1	0	$\Delta N \neq 0$ for $K_c' \to K_c'' = 0$

molecular symmetry (MS) group [12]. For bent ATMs with prolate rotational structure (i.e. $A > B > C$), the two choices of irreducible representations (irreps) in the C_s symmetry group (A', A'') map onto the parity $(+/-)$ of K_c for each rotational level, as seen in Table II. Each choice of $|N, |K_a\rangle$, for $|K_a| > 0$ therefore forms a parity doublet that is closely spaced and split by the rotational asymmetry $\Delta E \propto [A(B+C)-(B+C)^2]/[4(2A-B-C)]$ [13]. Note that this is analogous to the hyperfine and centrifugally induced parity-doubling in symmetric top molecules [14–17].

Combining rotational MS classifications with electronic and vibrational symmetries yields a total symmetry ($\Gamma_{\rm evr}$), which is expressed as $\Gamma_{\rm evr} = \Gamma_{\rm el} \times \Gamma_{\rm vib} \times \Gamma_{\rm rot}$. This gives rise to dipole parity selection rules, which require that the product symmetry of two $E1$-connected rovibronic states (Γ_1,Γ_2) transform as the electric dipole representation (Γ^*).

$$\Gamma_1 \times \Gamma_2 \subset \Gamma^* \tag{B2}$$

The representation Γ^* is odd under inversion. For the two most common ATM symmetry groups C_{2v} and C_s, this corresponds to A_2 and A'', respectively.

As summarized in Table II and III, selection rules for dipole transitions can be constructed based on both the parity and the orientation of the electronic TDM ($\hat{\mu}$) relative to the rotational bands. It was recently shown [11] that these selection rules can be leveraged to realize rotationally closed cycling schemes in a broad class of monovalent, open-shell ATMs using two or fewer RF sidebands. We find that these principles can be readily extended for closing cycling transitions in multivalent closed-shell and high-spin systems, including mixed-character intercombination lines.

1. Singlet Ground States: Group 13

For singlet group 13 molecules, spin-orbit mixing causes the $\tilde{X}^1A' \to \tilde{b}^3A''$ intercombination line to take on the character of the dipole-allowed $\tilde{X}^1A' \to \tilde{A}^1A'$ transition. This is a hybrid ab-type band, due to mixed alignment of the TDM with the two in-plane principal axes. The intermediate $\tilde{b}^3A'' \to \tilde{a}^3A'$ decay, meanwhile, is a dipole-allowed c-type band, with the TDM aligned with the out-of-plane axis. This band follows c-type rotational selection rules.

The high-spin character of the nuclei of most group 13 isotopes requires tailored study of rotational and hyperfine branching to determine a suitable cycling scheme. To illustrate general principles, we perform an analysis given a ^{27}Al cycling center, which has nuclear spin $I = 5/2$. In open-shell and high-spin manifolds of asymmetric tops, spin-rotation (including spin-orbit) interactions split each N_{K_a,K_c} rotational level into multiple $J = N + S$ branches. For the excited triplet manifolds of AlSH, each rotational level is split into three branches, $J = N-1, N$, and $N+1$. The level diagrams in Fig. 5 classify each rotational branch in terms of $\Gamma_{\rm evr}$ for vibrationless cycling states. The hyperfine state including the ^{27}Al spin $I(^{27}\text{Al})$ is denoted $F_1 = J + I(^{27}\text{Al})$, while total hyperfine spin including hydrogen spin $I(^1\text{H})$ is denoted $F_2 = F_1 + I(^1\text{H})$.

Overlaid arrows in figure 5 depict rotational closure schemes for vibrationless cycling and repump transitions in AlSH. The red, solid line depicts the main cycling transition between the $\tilde{X}^1A'$ ground state and the $\tilde{b}^3A''$ upper state. Due to the out-of-plane character of the excited state, the intercombination cycling line must be driven with even ΔK_c to respect parity, which are expected to override the (approximate) ab-type angular momentum selection rules in table III to yield $\Delta K_a = 0, \pm 1$ and $\Delta K_c = 0$ lines [18]. A rotationally closed cycling scheme for vibrationless and even-parity vibrational transitions can therefore be constructed by driving $F \to F-1$ ("type II") lines from $\tilde{X}^1A'\,|1_{01}, 1, 3/2, 1\rangle$, $|1_{11}, 1, 3/2, 1\rangle$, and $|2_{11}, 1, 3/2, 1\rangle$ to $\tilde{b}^3A''\,|1_{01}, 2, 1/2, 0\rangle$, where we adopt the $|N_{K_a,K_c}, J, F_1, F_2\rangle$ notation to describe angular angular momenta states. (Rotational schemes for repumping lines involving odd-parity vibrational transitions can be constructed using identical parity rules, while taking into account the symmetry of vibrational states ($\Gamma_{\rm vib}$) involved.)

By contrast, for decays from the $\tilde{b}^3A''$ upper state to the $\tilde{a}^3A'$ state, the usual spin-allowed dipole selection rules apply. As a c-type transition, the allowed lines obey parity and $\Delta K_a = \pm 1$ and $\Delta K_c = 0$ angular momentum selection rules. A rotationally closed repumping scheme from the $\tilde{a}^3A'$ state is depicted via thin, yellow dashed lines in figure 5. A total of eight hyperfine sidebands are implicated in the repumping pathways. For both the cycling and repumping schemes, rotational spacings are expected to be on the GHz-scale, while hyperfine and spin-rotation splittings will typically be on the 10 MHz - 1 GHz scale, making individual sidebands fully addressable via optical modulation with a manageable number of seed lasers [19]. Note that hyperfine-induced decays may populate other rotational states [20, 21]

2. Triplet Ground States: Group 15

For triplet group 15 molecules, the $\tilde{X}^3A'' \rightarrow \tilde{b}^1A''$ cycling line borrows intensity primarily from the $\tilde{X}^3A'' \rightarrow \tilde{A}^3A'$ spin-allowed c-type transition. Fig. 5 depicts the rotational closure scheme, including hyperfine effects, for the model system ^{31}PSH. Both the ^{31}P and proton nuclei have $I = 1/2$, and we define two hyperfine quantum numbers as $F_1 = J + I(^{31}\mathrm{P})$ and $F_2 = F_1 + I(^1H)$.

Because both states involved in the $\tilde{X}^3A'' \rightarrow \tilde{b}^1A''$ cycling line have the same electronic symmetry, parity rules require odd ΔK_c for vibrationless and even-parity vibrational transitions. We therefore expect that the allowed lines correspond to $\Delta K_a = 0, \pm 1$ and $\Delta K_c = 0$ rules. In the case of ^{31}PSH, driving from two ground rotational levels (1_{01}, 1_{11}), each with four hyperfine sidebands ($|0, 1/2, 1\rangle$, $|1, 1/2, 1\rangle$, $|1, 3/2, 1\rangle$, $|2, 3/2, 1\rangle$) is sufficient to close the main cycling line to the upper $\tilde{b}^1A''|0_{00}, 0, 1/2, 0\rangle$ state. Decays from $\tilde{b}^1A''|0_{00}, 0, 1/2, 0\rangle$ to the intermediate $\tilde{a}^1A'$ state are spin-allowed and obey c-type selection rules. Closure of the intermediate decay can be achieved by repumping the $|1_{10}, 1, 1/2, 1\rangle$ and $|1_{10}, 1, 3/2, 1\rangle$ sidebands in the $\tilde{a}^1A'$ state.

3. Doublet Ground States: Group 14

For doublet group 14 molecules, the $\tilde{X}^2A' \rightarrow \tilde{a}^4A''$ transition gains intensity primarily through spin-orbit mixing with the spin-allowed $\tilde{X}^2A' \rightarrow \tilde{B}^2A'$ and $\tilde{X}^2A' \rightarrow \tilde{C}^2A'$ ab-type transitions. The $\tilde{a}^4A'' \rightarrow \tilde{A}^2A''$ intermediate decay channel, meanwhile, gains intensity primarily through mixing with the $\tilde{A}^2A'' \rightarrow \tilde{B}^2A'$ c-type channel. As before, Fig. 5 depicts the rotational closure scheme, accounting hyperfine splittings, for ^{28}SiSH. The lack of a high-spin triplet electronic manifold, as well as the spin-0 character of the ^{28}Si nucleus is a simplifying factor, and we only define a single hyperfine number $F = J + I(^1\mathrm{H})$ associated with the addition of hydrogen spin.

Due to their intercombination character, only parity selection and overall angular momentum selection rules are expected to apply for the cycling and intermediate decay lines in ^{28}SiSH. For the cycling transition ($\tilde{X}^2A' \rightarrow \tilde{a}^4A''$), rotational closure (for parity-even vibrational transitions) can be achieved by driving type II transitions from three rotational states ($1_{01}, 1_{11}, 2_{11}$) and five spin-rotation components (with $F = 1$) in $\tilde{X}^2A'$ to $\tilde{a}^4A''|1_{01}, 1/2, 0\rangle$, where we denote the angular momentum states as $|N_{K_a,K_c}, J, F\rangle$. The intermediate decay channel can similarly be repumped by addressing three rotational states (0_{00}, 2_{02}, 2_{12}) and three $F = 1$ spin-rotation sidebands in $\tilde{A}^2A''$ to the $F = 0$ upper state.

[1] W. A. Goddard and L. B. Harding, The Description of Chemical Bonding From Ab Initio Calculations, Annual Review of Physical Chemistry **29**, 363 (1978).

[2] T. H. Dunning, L. T. Xu, T. Y. Takeshita, and B. A. Lindquist, Insights into the Electronic Structure of Molecules from Generalized Valence Bond Theory, The Journal of Physical Chemistry A **120**, 1763 (2016).

[3] T. Sano, Elementary Jacobi rotation method for generalized valence bond perfect-pairing calculations combined with simple procedure for generating reliable initial orbitals, Journal of Molecular Structure: THEOCHEM **528**, 177 (2000).

[4] J. Pipek and P. G. Mezey, A fast intrinsic localization procedure applicable for ab initio and semiempirical linear combination of atomic orbital wave functions, The Journal of Chemical Physics **90**, 4916 (1989).

[5] K. M. Ervin and W. C. Lineberger, Photoelectron spectra of dicarbon(1-) and ethynyl(1-), The Journal of Physical Chemistry **95**, 1167 (1991).

[6] J. C. J. Thynne and K. A. G. MacNeil, Negative ion formation by ethylene and 1,1-difluoroethylene, The Journal of Physical Chemistry **75**, 2584 (1971).

[7] S. E. Bradforth, E. H. Kim, D. W. Arnold, and D. M. Neumark, Photoelectron spectroscopy of CN^-, NCO^-, and NCS^-, The Journal of Chemical Physics **98**, 800 (1993).

[8] H.-J. Zhai, L.-M. Wang, S.-D. Li, and L.-S. Wang, Vibrationally Resolved Photoelectron Spectroscopy of BO^- and BO_2^-: A Joint Experimental and Theoretical Study, The Journal of Physical Chemistry A **111**, 1030 (2007).

[9] F. Breyer, P. Frey, and H. Hotop, High resolution photoelectron spectrometry of negative ions: Rotational transitions in laser-photodetachment of OH^-, SH^-, SD^-, Zeitschrift für Physik A Atoms and Nuclei **300**, 7 (1981).

[10] M. DeWitt, M. C. Babin, and D. M. Neumark, High-Resolution Photoelectron Spectroscopy of Vibrationally Excited OH^-, The Journal of Physical Chemistry A **125**, 7260 (2021).

[11] B. L. Augenbraun, J. M. Doyle, T. Zelevinsky, and I. Kozyryev, Molecular Asymmetry and Optical Cycling: Laser Cooling Asymmetric Top Molecules, Physical Review X **10**, 031022 (2020).

[12] P. R. Bunker and P. Jensen, *Molecular Symmetry and Spectroscopy*, 2nd ed. (NRC Research Press, Ottowa, 2006).

[13] S. R. Polo, Energy Levels of Slightly Asymmetric Top Molecules, Canadian Journal of Physics **35**, 880 (1957).

[14] H. H. Nielsen and D. M. Dennison, Anomalous Values of Certain of the Fine Structure Lines in the Ammonia Microwave Spectrum, Physical Review **72**, 86 (1947).

[15] G. R. Gunther-Mohr, C. H. Townes, and J. H. Van Vleck, Hyperfine Structure in the Spectrum of N 14 H 3 . II. Theoretical Discussion, Physical Review **94**, 1191 (1954).

[16] J. K. G. Watson, The symmetry condition for a first-

(a) AlF

$\tilde{X}^1\Sigma^+$	Calc.	Exp.	Err.
r_0	1.674744 Å	1.65436(2) Å[22]	+1.23%
ω_0	786.66 cm^{-1}	802.85(25) cm^{-1} [22]	−2.01%
d_0	1.5321 D	1.515(4) D [23]	+1.12%
$\tilde{a}^3\Pi$			
r_0	1.6687 Å	1.6476 Å[24]	+1.28%
ω_0	812.89 cm^{-1}	830.3(3) cm^{-1} [25]	−2.10%
τ	13.56 ms	13.3(29) ms [26],[a]	+1.95%
d_0	1.8476 D	1.780(3) D [23]	+3.78%
T_0	26320.276 cm^{-1}	27255.15(2) cm^{-1} [23]	−3.43%
$\tilde{A}^1\Pi$			
r_0	1.6680 Å	1.6485 Å[24]	+1.95%
ω_0	791.52 cm^{-1}	803.9(5) cm^{-1} [27]	−1.54%
τ	1.873 ns	1.90(3) ns [23]	−1.42%
d_0	1.4609 D	1.45(2) D [23]	+0.75%
T_0	43875.173 cm^{-1}	43950.285(10) cm^{-1} [23]	−0.17%

(b) AlOH

$\tilde{X}^1A'$	Calc.	Exp.	Err.
r_0(Al-O)	1.6924 Å	1.682 Å[29]	+0.62%
r_0(O-H)	0.9498 Å	0.878 Å[29], [a]	+8.18%
∠(Al-O-H)	157.54 Å	∼ 160°[29], [b]	–
ω(Al-O)	834.10 cm^{-1}	810.7 cm^{-1} [34]	+2.89%
ω(O-H)	4035.31 cm^{-1}	3787.0 cm^{-1} [34]	+6.56%
$\tilde{A}^1A'$			
ω(Al-O)	743.36 cm^{-1}	807.6 cm^{-1} [33]	−7.95%
ω(O-H)	3867.45 cm^{-1}	3258.4 cm^{-1} [33]	+18.7%
ω(bend)	624.80 cm^{-1}	636.6 cm^{-1} [33]	−1.85%
T_0	39810 cm^{-1}	40073 cm^{-1} [33]	−0.65%
$\tilde{B}^1A''$			
ω(Al-O)	747.55 cm^{-1}	760.3 cm^{-1} [33]	−1.68%
ω(bend)	598.92 cm^{-1}	581.0 cm^{-1} [33]	+3.08%
T_0	41550 cm^{-1}	41747 cm^{-1} [33]	−0.47%

(c) AlSH

$\tilde{X}^1A'$	Calc.	Exp.	Err.
r_0(Al-S)	2.2646 Å	2.240(6) Å[28]	+1.07%
r_0(S-H)	1.3464 Å	1.36(4) Å[28]	−1.00%
∠(Al-S-H)	90.19°	88.5±5.8°[28]	+1.91%

[a] Ω-averaged lifetime determined by measurements of the $a^3\Pi_1$ and $a^3\Pi_0$ states of AlF in [26]

[a] The experimentally determined O-H bond length is unusually short, which is suggested in [29] to be an artifact of large amplitude vibrations in the observed states.

[b] Inferred in [29] from experimentally determined bond lengths and comparisons against theoretical predictions [30, 31] of a bent ground state with a low barrier to quasi-linearity [32]. This is consistent with rotational [29] and photonionization spectra [33], which suggest that AlOH is, on average, a near-linear molecule with large-amplitude zero point bending.

Table IV. Calculated and experimental molecular constants for (a) AlF, (b) AlOH, and (c) AlSH. As described in the main text, ab initio values are calculated using the EOM-EE-CCSD method with aug-cc-pVTZ basis sets. Spin-orbit data (for estimating lifetimes of metastable states) is computed perturbatively using a Breit-Pauli Hamiltonian.

order Stark effect, Journal of Molecular Spectroscopy **50**, 281 (1974).

[17] W. Klemperer, K. K. Lehmann, J. K. G. Watson, and S. C. Wofsy, Can molecules have permanent electric dipole moments?, The Journal of Physical Chemistry **97**, 2413 (1993).

[18] J. T. Hougen, Rotational Structure of Singlet-Triplet Transitions in Near-Symmetric Tops, Canadian Journal of Physics **42**, 443 (1964).

[19] C. M. Holland, Y. Lu, and L. W. Cheuk, Synthesizing optical spectra using computer-generated holography techniques, New Journal of Physics **23**, 033028 (2021).

[20] E. B. Norrgard, E. R. Edwards, D. J. McCarron, M. H. Steinecker, D. DeMille, S. S. Alam, S. K. Peck, N. S. Wadia, and L. R. Hunter, Hyperfine structure of the $B^3\Pi_1$ state and predictions of optical cycling behavior in the $X \to B$ transition of TlF, Physical Review A **95**, 062506 (2017).

[21] N. J. Fitch and M. R. Tarbutt, Laser-cooled molecules, in *Advances In Atomic, Molecular, and Optical Physics*, Vol. 70, edited by L. F. Dimauro, H. Perrin, and S. F. Yelin (Academic Press, 2021) pp. 157–262.

[22] F. C. Wyse, W. Gordy, and E. F. Pearson, Millimeter and Submillimeter Wave Spectrum and Molecular Constants of Aluminum Monofluoride, The Journal of Chemical Physics **52**, 3887 (1970).

[23] S. Truppe, S. Marx, S. Kray, M. Doppelbauer, S. Hofsäss, H. C. Schewe, N. Walter, J. Pérez-Ríos, B. G. Sartakov, and G. Meijer, Spectroscopic characterization of aluminum monofluoride with relevance to laser cooling and trapping, Physical Review A **100**, 052513 (2019).

[24] G. Herzberg and K. P. Huber, *Molecular Spectra and Molecular Structure Volume IV: Constants of Diatomic Molecules* (Van Nostrand Reinhold, New York, NY, 1979).

[25] I. Kopp, B. Lindgren, and C. Malmberg, Rotational analysis of the $a^3\Pi - X^1\Sigma^+$ transition of AlF, Physica Scripta **14**, 170–174 (1976).

[26] N. Walter, M. Doppelbauer, S. Marx, J. Seifert, X. Liu, J. Pérez-Ríos, B. G. Sartakov, S. Truppe, and G. Meijer, Spectroscopic characterization of the $a^3\Pi$ state of aluminum monofluoride, The Journal of Chemical Physics **156**, 124306 (2022).

[27] H. C. Rowlinson and R. F. Barrow, The Absorption Spectrum of Aluminium Monofluoride in the Schumann Region, Proceedings of the Physical Society. Section A **66**, 771 (1953).

[28] A. Janczyk and L. M. Ziurys, Laboratory detection and pure rotational spectrum of AlSH ($\tilde{X}^1A$), The Astrophysical Journal **639**, L107–L110 (2006).

[29] A. J. Apponi, W. L. Barclay, Jr., and L. M. Ziurys, The millimeter-wave spectrum of AlOH, The Astrophysical Journal Letters **414**, L129 (1993).

[30] G. Vacek, B. J. DeLeeuw, and H. F. Schaefer, The $\tilde{X}$

AlOH–$\tilde{X}$ HAlO isomerization potential energy hypersurface, The Journal of Chemical Physics **98**, 8704 (1993).

[31] T. Trabelsi and J. S. Francisco, Is AlOH the Astrochemical Reservoir Molecule of AlO?: Insights from Excited Electronic States, The Astrophysical Journal **863**, 139 (2018).

[32] S. Li, K. W. Sattelmeyer, Y. Yamaguchi, and H. F. Schaefer, Characterization of the three lowest-lying singlet electronic states of AlOH, The Journal of Chemical Physics **119**, 12830 (2003).

[33] J. S. Pilgrim, D. L. Robbins, and M. A. Duncan, Photoionization electronic spectroscopy of AlOH, Chemical Physics Letters **202**, 203 (1993).

[34] X. Wang and L. Andrews, Infrared Spectroscopic Observation of the Group 13 Metal Hydroxides, $M(OH)_{1,2,3}$ (M = Al, Ga, In, and Tl) and $HAl(OH)_2$, The Journal of Physical Chemistry A **111**, 1860 (2007).

[35] A. E. Reed, R. B. Weinstock, and F. Weinhold, Natural population analysis, The Journal of Chemical Physics **83**, 735 (1985).

[36] G. Knizia, Intrinsic Atomic Orbitals: An Unbiased Bridge between Quantum Theory and Chemical Concepts, Journal of Chemical Theory and Computation **9**, 4834 (2013).

[37] C. M. Breneman and K. B. Wiberg, Determining atom-centered monopoles from molecular electrostatic potentials. The need for high sampling density in formamide conformational analysis, Journal of Computational Chemistry **11**, 361 (1990).

[38] U. C. Singh and P. A. Kollman, An approach to computing electrostatic charges for molecules, Journal of Computational Chemistry **5**, 129 (1984).

[39] B. H. Besler, K. M. Merz Jr., and P. A. Kollman, Atomic charges derived from semiempirical methods, Journal of Computational Chemistry **11**, 431 (1990).

[40] E. D. Glendening, J. K. Badenhoop, A. E. Reed, J. E. Carpenter, J. A. Bohmann, C. M. Morales, and F. Weinhold, NBO 5.0, Theoretical Chemistry Institute, University of Wisconsin (2001).

Table S1. Electronic energies (eV), rovibrational constants (cm^{-1}), and geometries (Å, degrees) for group 13 MSH molecules considered in Section II.

BSH	ΔE	r(B-S)	r(S-H)	$\angle$(B-S-H)	A	B	C	v_1	v_2	v_3
$\tilde{X}^1A'$	–	1.822	1.348	87.65	9.492	0.616	0.579	587.07	774.14	2676.45
$\tilde{a}^3A'$	1.461	1.736	1.357	102.50	9.981	0.668	0.626	845.59	936.26	2534.03
$\tilde{b}^3A''$	2.396	1.837	1.347	89.21	9.512	0.605	0.569	464.17	757.76	2693.52
$\tilde{A}^1A'$	3.694	1.705	1.407	105.90	9.623	0.687	0.641	815.13	939.58	1935.49
$\tilde{B}^1A''$ [a]	4.122	1.871	1.348	88.60	9.501	0.584	0.550	783.63i	496.84	2049.82
$\tilde{c}^3A'$	4.759	1.892	1.829	179.84	–	0.4870	–	187.75	565.26	801.93
$\tilde{C}^1A'$	4.918	2.563	1.347	86.48	9.535	0.311	0.302	297.31	336.29	2692.98
AlSH	ΔE	r(Al-S)	r(S-H)	$\angle$(Al-S-H)	A	B	C	v_1	v_2	v_3
$\tilde{X}^1A'$	–	2.264	1.346	90.19	9.523	0.221	0.216	426.18	496.56	2684.52
$\tilde{a}^3A'$	2.340	2.203	1.344	98.59	9.833	0.233	0.227	428.68	502.46	2701.20
$\tilde{b}^3A''$	2.744	2.259	1.346	90.09	9.522	0.222	0.217	429.62	497.47	2684.65
$\tilde{A}^1A'$	3.694	2.260	1.351	100.29	9.835	0.216	0.221	433.35	486.85	2649.27
$\tilde{B}^1A''$	4.097	2.404	1.347	89.30	9.514	0.193	0.197	325.03	497.52	2681.22
$\tilde{c}^3A'$	4.161	2.899	1.347	89.88	9.512	0.135	0.133	17.48	478.35	2677.03
$\tilde{C}^1A'$ [a]	4.381	3.153	1.346	90.27	9.520	0.114	0.113	107.77i	457.08	2679.83
GaSH	ΔE	r(Ga-S)	r(S-H)	$\angle$(Ga-S-H)	A	B	C	v_1	v_2	v_3
$\tilde{X}^1A'$	–	2.293	1.345	90.21	9.539	0.144	0.142	346.65	490.68	2691.94
$\tilde{a}^3A'$	2.699	2.207	1.345	98.98	9.835	0.154	0.152	375.87	701.43	2664.27
$\tilde{b}^3A''$	3.113	2.283	1.346	89.66	9.531	0.145	0.143	327.39	616.18	2694.97
$\tilde{B}^1A''$	3.969	2.819	1.348	105.57	10.316	0.0943	0.0934	147.42	279.02	2655.63
$\tilde{c}^3A'$	3.999	3.542	1.344	179.99	–	0.0585	–	61.57	338.55	2712.45
$\tilde{C}^1A'$	4.167	3.152	1.347	88.18	9.517	0.144	0.142	113.60	201.60	2692.19
InSH	ΔE	r(In-S)	r(S-H)	$\angle$(In-S-H)	A	B	C	v_1	v_2	v_3
$\tilde{X}^1A'$	–	2.503	1.345	91.06	9.549	0.105	0.104	300.29	472.56	2691.19
$\tilde{a}^3A'$	2.616	2.423	1.343	96.96	9.753	0.112	0.110	316.66	642.26	2698.88
$\tilde{b}^3A''$	2.921	2.485	1.345	90.11	9.538	0.106	0.105	283.35	594.64	2696.07
$\tilde{A}^1A'$	3.556	2.602	1.345	96.08	9.675	0.0968	0.0959	160.14	530.21	2684.08
$\tilde{c}^3A'$	3.719	3.854	1.343	179.98	–	0.0432	–	33.38	367.44	2717.21
$\tilde{B}^1A''$	3.745	3.132	1.346	87.95	9.535	0.0671	0.0667	33.76	257.11	2702.37
$\tilde{C}^1A'$	3.885	3.336	1.347	89.94	9.516	0.0591	0.0587	67.55	136.48	2692.06
TlSH	ΔE	r(Tl-S)	r(S-H)	$\angle$(Tl-S-H)	A	B	C	v_1	v_2	v_3
$\tilde{X}^1A'$	–	2.576	1.345	91.08	9.554	0.0893	0.0885	272.59	454.01	2692.25
$\tilde{a}^3A'$	3.100	2.541	1.344	97.10	9.740	0.0915	0.0907	212.35	560.94	2691.48
$\tilde{b}^3A''$	3.330	2.661	1.345	88.65	9.536	0.0838	0.0831	157.92	510.66	2701.71
$\tilde{A}^1A'$	3.512	2.968	1.345	95.09	9.635	0.0672	0.0667	71.31	275.75	2699.78
$\tilde{c}^3A'$	3.538	3.170	1.347	86.88	9.527	0.0591	0.0587	106.87	197.40	2692.33
$\tilde{B}^1A''$	3.563	3.103	1.346	105.11	10.280	0.0612	0.0608	118.94	202.09	2678.72
$\tilde{C}^1A'$	3.704	3.388	1.347	89.60	9.515	0.0517	0.0514	87.27	162.82	2692.33

[a] State is unbound and pre-dissociative. Geometry and energies correspond to saddlepoints on the potential energy surface.

Table S2. Electronic energies (eV), rovibrational constants (cm^{-1}), and geometries (Å, degrees) for group 14 MSH molecules considered in Section II.

CSH	ΔE	r(C-S)	r(S-H)	$\angle$(C-S-H)	A	B	C	v_1	v_2	v_3
$\tilde{X}^2A'$	–	1.664	1.361	101.64	9.855	0.637	0.682	805.80	921.01	2512.34
$\tilde{A}^2A''$	1.085	1.767	1.351	85.21	9.488	0.616	0.578	586.73	774.00	2662.54
$\tilde{a}^4A''$	2.121	1.720	1.347	97.67	9.761	0.602	0.642	802.76	942.57	2650.00
$\tilde{B}^2A'$	3.488	1.352	1.755	98.47	9.746	0.616	0.579	729.04	930.90	2627.00
$\tilde{C}^2A'$	4.380	1.772	1.425	114.79	10.679	0.589	0.558	236.54	955.64	2031.77
SiSH	ΔE	r(Si-S)	r(S-H)	$\angle$(Si-S-H)	A	B	C	v_1	v_2	v_3
$\tilde{X}^2A'$	–	2.128	1.346	99.73	9.865	0.243	0.237	516.11	681.41	2667.08
$\tilde{A}^2A''$	0.593	2.197	1.347	88.20	9.497	0.230	0.225	466.37	566.04	2675.51
$\tilde{a}^4A''$	2.646	2.187	1.344	96.01	9.705	0.226	0.232	434.40	739.17	2696.67
$\tilde{B}^2A'$	3.793	2.120	1.355	103.01	10.003	0.245	0.239	417.60	827.97	2556.84
$\tilde{C}^2A'$	3.894	2.640	1.349	103.33	10.103	0.158	0.156	263.62	363.54	2673.15
GeSH	ΔE	r(Ge-S)	r(S-H)	$\angle$(Ge-S-H)	A	B	C	v_1	v_2	v_3
$\tilde{X}^2A'$	–	2.209	1.345	98.69	9.830	0.148	0.150	410.73	654.91	2680.73
$\tilde{A}^2A''$	0.525	2.271	1.347	89.28	9.513	0.141	0.143	384.28	557.66	2681.62
$\tilde{a}^4A''$	2.845	2.324	1.344	95.86	9.690	0.134	0.136	242.58	649.39	2700.67
$\tilde{B}^2A'$	3.042	3.019	1.345	93.50	9.595	0.0810	0.0803	75.02	272.28	2707.13
$\tilde{C}^2A'$	3.670	2.755	1.347	101.41	9.963	0.0968	0.0958	146.72	350.71	2687.71

Table S3. Electronic energies (eV), rovibrational constants (cm^{-1}), and geometries (Å, degrees) for group 15 MSH molecules considered in Section II.

PSH	ΔE	r(P-S)	r(S-H)	$\angle$(P-S-H)	A	B	C	v_1	v_2	v_3
$\tilde{X}^3A''$	–	2.107	1.344	96.05	9.709	0.231	0.237	508.23	744.66	2693.56
$\tilde{a}^1A'$	0.325	1.991	1.359	105.02	10.157	0.256	0.263	600.19	889.94	2533.13
$\tilde{b}^1A''$	0.856	2.078	1.347	97.41	9.733	0.237	0.243	535.22	744.00	2659.74
$\tilde{A}^3A'$	3.468	2.223	1.362	107.95	10.432	0.206	0.210	413.65	710.99	2526.34
$\tilde{B}^3A''$ [a]	3.740	2.139	1.353	102.89	10.025	0.228	0.223	$457.26i$	450.37	2565.86
$\tilde{c}^1A'$	3.962	2.309	1.343	92.52	9.600	0.198	0.194	356.35	683.95	2698.57
AsSH	ΔE	r(As-S)	r(S-H)	$\angle$(As-S-H)	A	B	C	v_1	v_2	v_3
$\tilde{X}^3A''$	–	2.222	1.343	95.30	9.689	0.149	0.146	401.33	712.08	2703.94
$\tilde{a}^1A'$	0.475	2.114	1.352	103.57	10.090	0.163	0.160	495.79	716.90	2613.70
$\tilde{b}^1A''$	0.852	2.196	1.345	96.49	9.710	0.152	0.149	429.09	658.02	2662.37
$\tilde{A}^3A'$	3.193	2.518	1.342	86.22	9.605	0.116	0.115	249.63	457.25	2712.55
$\tilde{B}^3A''$	3.831	2.321	1.351	104.03	9.605	0.116	0.115	194.00	414.32	2727.01
$\tilde{c}^1A'$	3.788	2.508	1.341	86.59	9.607	0.117	0.116	247.95	638.28	2720.60
SbSH	ΔE	r(Sb-S)	r(S-H)	$\angle$(Sb-S-H)	A	B	C	v_1	v_2	v_3
$\tilde{X}^3A''$	–	2.427	1.342	94.71	9.672	0.110	0.109	353.07	671.24	2711.20
$\tilde{a}^1A'$	0.593	2.346	1.345	101.03	9.972	0.117	0.116	391.32	746.03	2670.33
$\tilde{b}^1A''$	0.790	2.410	1.343	95.58	9.692	0.112	0.110	363.68	666.81	2701.20
$\tilde{A}^3A'$	2.805	2.691	1.343	88.61	9.572	0.0899	0.0890	245.33	423.23	2707.10
$\tilde{B}^3A''$	3.681	2.551	1.347	102.06	10.011	0.0993	0.0983	297.11	551.80	2660.40
$\tilde{c}^1A'$	3.461	2.469	1.420	179.94	–	0.102	–	244.68	380.65	1935.27
BiSH	ΔE	r(Bi-S)	r(S-H)	$\angle$(Bi-S-H)	A	B	C	v_1	v_2	v_3
$\tilde{X}^3A''$	–	2.516	1.341	94.45	9.678	0.0931	0.0923	323.28	645.81	2717.71
$\tilde{a}^1A'$	0.658	2.440	1.343	100.18	9.944	0.0987	0.0978	354.46	706.33	2692.61
$\tilde{b}^1A''$	0.775	2.501	1.342	95.13	9.678	0.0931	0.0923	330.65	386.65	2705.49
$\tilde{A}^3A'$	2.583	2.774	1.342	88.69	9.580	0.0769	0.0763	231.47	334.45	2702.03
$\tilde{B}^3A''$	3.728	2.763	1.346	106.00	10.396	0.0768	0.0762	221.64	462.20	2678.71
$\tilde{c}^1A'$	3.111	2.309	1.341	87.77	9.590	0.0774	0.0767	232.26	379.37	2705.33

[a] State is unbound and pre-dissociative. Geometry and energies correspond to saddlepoints on the potential energy surface.

Table S4. Calculated Franck-Condon factors (FCFs) for eight leading vibronic decays for cycling transitions in multivalent molecules. Vibrational states are denoted with the shorthand convention $(v_1\, v_2\, v_3)$.

BSH		AlSH		GaSH		InSH	
$\tilde{b}^3A'' \to \tilde{X}^1A'$	FCF	$\tilde{b}^3A'' \to \tilde{X}^1A'$	FCF	$\tilde{b}^3A'' \to \tilde{X}^1A'$	FCF	$\tilde{b}^3A'' \to \tilde{X}^1A'$	FCF
(000) → (000)	0.9600	(000) → (000)	0.9974	(000) → (000)	0.9804	(000) → (000)	0.9517
(000) → (100)	0.01497	(000) → (100)	2.373×10^{-3}	(000) → (100)	0.01139	(000) → (100)	0.03719
(000) → (010)	0.01511	(000) → (010)	2.309×10^{-4}	(000) → (020)	5.910×10^{-3}	(000) → (020)	5.854×10^{-3}
(000) → (200)	7.835×10^{-3}	(000) → (101)	3.192×10^{-6}	(000) → (110)	8.691×10^{-4}	(000) → (010)	2.345×10^{-3}
(000) → (020)	4.236×10^{-4}	(000) → (011)	2.369×10^{-6}	(000) → (200)	6.751×10^{-4}	(000) → (200)	2.123×10^{-3}
(000) → (300)	3.093×10^{-4}	(000) → (200)	1.384×10^{-6}	(000) → (010)	5.467×10^{-4}	(000) → (120)	2.765×10^{-4}
(000) → (110)	1.467×10^{-4}	(000) → (110)	7.536×10^{-7}	(000) → (120)	8.754×10^{-5}	(000) → (011)	1.861×10^{-4}
(000) → (400)	9.401×10^{-5}	(000) → (020)	2.257×10^{-7}	(000) → (011)	6.548×10^{-5}	(000) → (110)	1.404×10^{-4}
$\tilde{b}^3A'' \to \tilde{a}^3A'$	FCF	$\tilde{b}^3A'' \to \tilde{a}^3A'$	FCF	$\tilde{b}^3A'' \to \tilde{a}^3A'$	FCF	$\tilde{b}^3A'' \to \tilde{a}^3A'$	FCF
(000) → (010)	0.2466	(000) → (000)	0.5645	(000) → (000)	0.3658	(000) → (000)	0.5455
(000) → (000)	0.1708	(000) → (010)	0.2485	(000) → (100)	0.2125	(000) → (100)	0.2076
(000) → (020)	4.980×10^{-3}	(000) → (020)	0.06006	(000) → (010)	0.1357	(000) → (010)	0.1084
(000) → (510)	6.612×10^{-3}	(000) → (110)	0.01666	(000) → (200)	0.07661	(000) → (200)	0.05159
(000) → (120)	6.115×10^{-3}	(000) → (030)	0.01311	(000) → (110)	0.06946	(000) → (110)	0.03542
(000) → (101)	5.978×10^{-3}	(000) → (101)	0.01020	(000) → (020)	0.03233	(000) → (020)	0.01413
(000) → (700)	5.719×10^{-3}	(000) → (111)	5.778×10^{-3}	(000) → (210)	0.02251	(000) → (300)	0.01023
(000) → (020)	4.980×10^{-3}	(000) → (120)	2.694×10^{-3}	(000) → (300)	0.02154	(000) → (210)	7.788×10^{-3}

TlSH		CSH		SiSH		GeSH	
$\tilde{b}^3A'' \to \tilde{a}^3A'$	FCF	$\tilde{a}^4A'' \to \tilde{X}^2A'$	FCF	$\tilde{a}^4A'' \to \tilde{X}^2A'$	FCF	$\tilde{a}^4A'' \to \tilde{X}^2A'$	FCF
(000) → (000)	0.5210	(000) → (000)	0.6667	(000) → (000)	0.7049	(000) → (000)	0.2498
(000) → (100)	0.2174	(000) → (100)	0.1855	(000) → (100)	0.2081	(000) → (100)	0.2508
(000) → (200)	0.1209	(000) → (010)	0.07485	(000) → (200)	0.05043	(000) → (200)	0.1979
(000) → (300)	0.05302	(000) → (110)	0.03172	(000) → (010)	0.01917	(000) → (300)	0.1307
(000) → (400)	0.02369	(000) → (200)	0.01888	(000) → (300)	0.01028	(000) → (400)	0.07796
(000) → (010)	0.01794	(000) → (020)	6.588×10^{-3}	(000) → (110)	2.614×10^{-3}	(000) → (500)	0.04304
(000) → (110)	0.01231	(000) → (210)	5.073×10^{-3}	(000) → (400)	1.909×10^{-3}	(000) → (600)	0.02243
(000) → (500)	9.774×10^{-3}	(000) → (120)	3.459×10^{-3}	(000) → (011)	1.174×10^{-3}	(000) → (700)	0.01116
$\tilde{b}^3A'' \to \tilde{a}^3A'$	FCF	$\tilde{a}^4A'' \to \tilde{X}^2A'$	FCF	$\tilde{a}^4A'' \to \tilde{X}^2A'$	FCF	$\tilde{a}^4A'' \to \tilde{X}^2A'$	FCF
(000) → (000)	0.2706	(000) → (000)	0.3412	(000) → (000)	0.7515	(000) → (000)	0.5631
(000) → (100)	0.2362	(000) → (100)	0.2235	(000) → (010)	0.2083	(000) → (100)	0.1894
(000) → (200)	0.1407	(000) → (010)	0.1691	(000) → (100)	0.01423	(000) → (010)	0.08689
(000) → (010)	0.07526	(000) → (110)	0.1067	(000) → (020)	0.01265	(000) → (200)	0.08541
(000) → (300)	0.06789	(000) → (020)	0.03838	(000) → (011)	5.485×10^{-3}	(000) → (300)	0.03029
(000) → (110)	0.05896	(000) → (120)	0.02814	(000) → (120)	2.550×10^{-3}	(000) → (300)	0.03029
(000) → (210)	0.03404	(000) → (120)	0.02323	(000) → (021)	2.135×10^{-3}	(000) → (110)	0.01331
(000) → (400)	0.02870	(000) → (111)	7.765×10^{-3}	(000) → (001)	1.159×10^{-3}	(000) → (400)	0.01097

PSH		AsSH		SbSH		BiSH	
$\tilde{b}^1A'' \to \tilde{X}^3A'$	FCF	$\tilde{b}^1A'' \to \tilde{X}^3A'$	FCF	$\tilde{b}^1A'' \to \tilde{X}^3A'$	FCF	$\tilde{b}^1A'' \to \tilde{X}^3A'$	FCF
(000) → (000)	0.9018	(000) → (000)	0.9224	(000) → (000)	0.9572	(000) → (000)	0.9674
(000) → (100)	9.074×10^{-2}	(100) → (000)	0.06913	(000) → (100)	0.03952	(000) → (020)	0.03050
(000) → (010)	3.852×10^{-3}	(000) → (010)	5.412×10^{-3}	(000) → (010)	2.684×10^{-3}	(000) → (040)	1.443×10^{-3}
(000) → (200)	2.506×10^{-3}	(000) → (020)	1.362×10^{-3}	(000) → (200)	3.351×10^{-4}	(000) → (011)	4.409×10^{-4}
(000) → (110)	6.621×10^{-4}	(000) → (110)	5.081×10^{-4}	(000) → (110)	2.042×10^{-4}	(000) → (060)	7.583×10^{-5}
(000) → (001)	2.229×10^{-4}	(000) → (200)	4.726×10^{-4}	(000) → (011)	7.613×10^{-5}	(000) → (200)	7.041×10^{-5}
(000) → (011)	1.648×10^{-4}	(000) → (011)	2.257×10^{-4}	(000) → (001)	2.977×10^{-5}	(000) → (110)	4.556×10^{-5}
(000) → (101)	4.968×10^{-5}	(000) → (210)	2.208×10^{-4}	(000) → (020)	1.709×10^{-5}	(000) → (031)	4.171×10^{-5}
$\tilde{b}^1A'' \to \tilde{a}^1A'$	FCF	$\tilde{b}^1A'' \to \tilde{a}^1A'$	FCF	$\tilde{b}^1A'' \to \tilde{a}^1A'$	FCF	$\tilde{b}^1A'' \to \tilde{a}^1A'$	FCF
(000) → (000)	0.2986	(000) → (000)	0.2690	(000) → (000)	0.5130	(000) → (000)	0.3994
(000) → (100)	0.2954	(000) → (100)	0.2780	(000) → (100)	0.2797	(000) → (100)	0.3044
(000) → (200)	0.1633	(000) → (200)	0.1616	(000) → (200)	0.08656	(000) → (200)	0.1267
(000) → (300)	0.06617	(000) → (300)	0.06906	(000) → (010)	0.05086	(000) → (300)	0.03802
(000) → (010)	0.04189	(000) → (010)	0.06129	(000) → (110)	0.02369	(000) → (020)	0.02171
(000) → (110)	0.03943	(000) → (110)	0.05213	(000) → (300)	0.01983	(000) → (010)	0.02093
(000) → (400)	0.02183	(000) → (210)	0.02505	(000) → (210)	6.316×10^{-3}	(000) → (120)	0.01669
(000) → (210)	0.02083	(000) → (400)	0.02412	(000) → (020)	5.834×10^{-3}	(000) → (110)	0.01638

Table S5. Computed mean-field Breit-Pauli spin-orbit matrix elements (cm^{-1}) for group 13 MSH molecules with respect to spin-electronic states $|\Lambda, \Sigma\rangle$.

Matrix Element	BSH	AlSH	GaSH	InSH	TlSH
$\langle \tilde{X}^1A', 0\|\hat{H}_{\rm SO}\|\tilde{b}^3A'', \pm1\rangle$	$-34.041e^{\mp0.964i}$	$43.203e^{\pm1.333i}$	$172.641e^{\pm3.563i}$	$518.827e^{\pm9.871i}$	$209.677e^{\mp6140.860i}$
$\langle \tilde{A}^1A', 0\|\hat{H}_{\rm SO}\|\tilde{b}^3A'', \pm1\rangle$	$-5.078e^{\mp6.332i}$	$2.821e^{\mp28.488i}$	$-4.5965e^{\pm202.794i}$	$25.886e^{\mp793.378i}$	$5212.156e^{\pm332.300i}$
$\langle \tilde{B}^1A'', 0\|\hat{H}_{\rm SO}\|\tilde{a}^3A', \pm1\rangle$	$-2.485e^{\pm8.770i}$	$0.0863e^{\mp29.389i}$	$10.439e^{\mp205.505i}$	$32.190e^{\mp806.937i}$	$-5123.191e^{\mp216.603i}$
$\langle \tilde{C}^1A', 0\|\hat{H}_{\rm SO}\|\tilde{b}^3A', \pm1\rangle$	$7.992e^{\mp30.267i}$	$5.388e^{\pm16.171i}$	$23.325e^{\mp9.280i}$	$257.066e^{\pm31.535i}$	$-5206.329e^{\mp540.624i}$
	CSH	SiSH	GeSH		
$\langle \tilde{X}^2A', \pm\frac{1}{2}\|\hat{H}_{\rm SO}\|\tilde{a}^4A'', \pm\frac{3}{2}\rangle$	$51.645e^{\pm8.795i}$	$-71.321e^{\mp5.719i}$	$64.008e^{\pm6.129i}$		
$\langle \tilde{X}^2A', \pm\frac{1}{2}\|\hat{H}_{\rm SO}\|\tilde{a}^4A'', \mp\frac{1}{2}\rangle$	$29.817e^{\mp5.078i}$	$-41.177e^{\mp3.302i}$	$36.955e^{\mp3.538i}$		
$\langle \tilde{B}^2A', \pm\frac{1}{2}\|\hat{H}_{\rm SO}\|\tilde{a}^4A'', \pm\frac{3}{2}\rangle$	$15.329e^{\pm4.737i}$	$12.027e^{\mp60.937i}$	$13.746e^{\pm32.229i}$		
$\langle \tilde{B}^2A', \pm\frac{1}{2}\|\hat{H}_{\rm SO}\|\tilde{a}^4A'', \mp\frac{1}{2}\rangle$	$8.850e^{\mp2.735i}$	$6.944e^{\pm35.182i}$	$7.936e^{\mp18.608i}$		
$\langle \tilde{C}^2A', \pm\frac{1}{2})\|\hat{H}_{\rm SO}\|\tilde{a}^4A'', \pm\frac{3}{2})\rangle$	$4.635e^{-20.198i}$	$80.457e^{-12.007i}$	$93.260e^{12.370i}$		
$\langle \tilde{C}^2A', \pm\frac{1}{2}\|\hat{H}_{\rm SO}\|\tilde{a}^4A'', \mp\frac{1}{2}\rangle$	$86.181e^{23.323}$	$92.904e^{-13.864i}$	$-107.687e^{14.284i}$		
	PSH	AsSH	SbSH	BiSH	
$\langle \tilde{X}^3A'', \pm1\|\hat{H}_{\rm SO}\|\tilde{a}^1A', 0\rangle$	$-2.608e^{\mp103.992i}$	$12.889e^{\mp592.464i}$	$-42.417e^{\pm1880.700i}$	$10272.392e^{\pm247.815i}$	
$\langle \tilde{A}^3A', \pm1\|\hat{H}_{\rm SO}\|\tilde{b}^1A'', 0\rangle$	$16.024e^{\pm13.687i}$	$372.723e^{\pm37.734i}$	$1289.094e^{\pm52.616i}$	$-368.162e^{\mp8585.580i}$	
$\langle \tilde{B}^3A'', \pm1\|\hat{H}_{\rm SO}\|\tilde{a}^1A', 0\rangle$	$117.880e^{\pm9.027i}$	$-428.892e^{\pm4.021i}$	$1162.687e^{\pm0.326}$	$-7077.983e^{\pm166.707i}$	
$\langle \tilde{C}^3A', \pm1\|\hat{H}_{\rm SO}\|\tilde{b}^1A'', 0\rangle$	–	$-16.942e^{\pm114.620i}$	$902.415e^{\pm31.278i}$	–	

Table S6. Calculated moments (in Debye) for spin-allowed dipole transitions in multivalent MSH molecules

Transition	Orientation	BSH	AlSH	GaSH	InSH	TlSH
$d_0(\tilde{X}^1A')$	*ab*-type	1.7644	1.3585	1.8616	2.7739	3.7892
$\tilde{X}^1A' \rightarrow \tilde{A}^1A'$	*ab*-type	1.5059	2.5257	1.9927	2.1981	1.4057
$\tilde{X}^1A' \rightarrow \tilde{B}^1A''$	*c*-type	1.5052	2.6114	1.9376	2.1372	1.3434
$\tilde{X}^1A' \rightarrow \tilde{C}^1A'$	*ab*-type	1.5051	0.3171	0.9196	0.7434	0.9694
$\tilde{a}^3A' \rightarrow \tilde{b}^3A''$	*c*-type	0.06753	0.02584	0.029131	0.01351	0.005602
		CSH	SiSH	GeSH		
$d_0(\tilde{X}^2A')$	*ab*-type	1.4663	0.8947	1.3986		
$\tilde{X}^2A' \rightarrow \tilde{A}^2A''$	*c*-type	0.1008	0.02842	0.02842		
$\tilde{A}^2A'' \rightarrow \tilde{B}^2A'$	*c*-type	0.02508	0.2094	0.2551		
$\tilde{A}^2A'' \rightarrow \tilde{C}^2A'$	*c*-type	0.1474	0.07286	0.03832		
		PSH	AsSH	SbSH	BiSH	
$d_0(\tilde{X}^3A'')$	*ab*-type	0.8065	0.9317	1.3588	2.0861	
$\tilde{X}^3A'' \rightarrow \tilde{A}^3A'$	*c*-type	0.30537	0.3776	0.1753	0.4578	
$\tilde{X}^3A'' \rightarrow \tilde{B}^3A''$	*ab*-type	0.67851	0.6206	0.6950	0.4795	
$\tilde{X}^3A'' \rightarrow \tilde{C}^3A'$	*c*-type	0.29843	0.07096	0.0712	0.06363	
$\tilde{a}^1A' \rightarrow \tilde{b}^3A''$	*c*-type	0.06075	0.05008	0.03274	0.02700	

Table S7. Calculated atomic partial charges for AlXH systems (X=O, S, Se, Te, Po) using orbital-based (Mulliken, NAO [35], IAO [36]) and electrostatic potential-based (CHELPG [37], Merz-Kollman [38, 39]) methods. Charges on atomic center i are denoted Q_i, while the charge difference between the Al and X chalogen center are denoted $\Delta Q_{\text{Al-X}}$. NAO/NPA charges are computed using the NBO 5.0 package [40].

Method	Molecule	Q_{Al}	Q_{X}	Q_{H}	$\Delta Q_{\text{Al-X}}$
Mulliken	AlOH	0.3718	-0.6740	0.3022	1.0458
	AlSH	0.2517	-0.4105	0.1588	0.6621
	AlSeH	0.2208	-0.1519	-0.0689	0.3728
	AlTeH	0.1499	0.0149	-0.1648	0.1350
	AlPoH	0.1191	0.0541	-0.1732	0.0649
NAO (NPA)	AlOH	0.8750	-1.3887	0.5137	2.2637
	AlSH	0.7002	-0.8216	0.1215	1.5218
	AlSeH	0.6601	-0.7191	0.0590	1.3793
	AlTeH	0.5949	-0.5436	-0.0513	1.1384
	AlPoH	0.5704	-0.4889	-0.0815	1.0593
IAO (IPA)	AlOH	0.5395	-0.9160	0.3765	1.4555
	AlSH	0.3595	-0.4368	0.0774	0.7963
	AlSeH	0.3153	-0.3459	0.0306	0.6612
	AlTeH	0.2502	-0.1995	-0.0508	0.4497
	AlPoH	0.2356	-0.1699	-0.0657	0.4056
CHELPG	AlOH	0.0762	-0.2879	0.2117	0.3641
	AlSH	0.1531	-0.2768	0.1237	0.4298
	AlSeH	0.1570	-0.2465	0.0895	0.4035
	AlTeH	0.1606	-0.1940	0.0334	0.3546
	AlPoH	0.1397	-0.1248	-0.0148	0.2645
Merz-Kollman	AlOH	0.0610	-0.3018	0.2408	0.3628
	AlSH	0.1371	-0.2738	0.1367	0.4109
	AlSeH	0.1414	-0.2392	0.0979	0.3806
	AlTeH	0.1471	-0.1906	0.0435	0.3377
	AlPoH	0.1324	-0.1296	-0.0028	0.2620

Table S8. Spin-contamination indices for Group 14 MSH calculations. Listed are calculated and spin-pure $\langle S^2 \rangle$ values for high-spin ($m_s = 3/2$) unrestricted Hartree-Fock (UHF) and CCSD references at CCSD-optimized equilibrium geometries for the $\tilde{a}^4A''$ state, and the same values for low spin ($m_s = 1/2$) EOM-SF-CCSD targets generated via response calculation at the CCSD-optimized $\tilde{X}^2A''$ geometry.

Molecule	State	$\langle S^2 \rangle$ calculated	$\langle S^2 \rangle$ pure	$\langle S^2 \rangle$ deviation
CSH	UHF states (relaxed)			
	$\tilde{a}^4A''$ ($m_s = 3/2$)	3.769	3.750	0.51%
	CCSD/UHF states (relaxed)			
	$\tilde{a}^4A''$ ($m_s = 3/2$)	3.751	3.750	0.03%
	EOM-SF-CCSD/UHF states (response)			
	X^2A' ($m_s = 1/2$)	0.763	0.750	1.72%
	$\tilde{A}^2A''$ ($m_s = 1/2$)	0.757	0.750	0.96%
	$\tilde{B}^2A'$ ($m_s = 1/2$)	0.779	0.750	3.85%
	$\tilde{C}^2A'$ ($m_s = 1/2$)	0.797	0.750	6.21%
	$\tilde{a}^4A''$ ($m_s = 1/2$)	3.755	3.750	0.13%
SiSH	UHF states (relaxed)			
	$\tilde{a}^4A''$ ($m_s = 3/2$)	3.761	3.750	0.29%
	CCSD/UHF states (relaxed)			
	$\tilde{a}^4A''$ ($m_s = 3/2$)	3.751	3.750	0.03%
	EOM-SF-CCSD/UHF states (response)			
	X^2A' ($m_s = 1/2$)	0.755	0.750	0.70%
	$\tilde{A}^2A''$ ($m_s = 1/2$)	0.752	0.750	0.31%
	$\tilde{B}^2A'$ ($m_s = 1/2$)	0.764	0.750	1.85%
	$\tilde{C}^2A'$ ($m_s = 1/2$)	0.764	0.750	1.86%
	$\tilde{a}^4A''$ ($m_s = 1/2$)	3.753	3.750	0.08%
GeSH	UHF states (relaxed)			
	$\tilde{a}^4A''$ ($m_s = 3/2$)	3.784	3.750	0.92%
	CCSD/UHF states (relaxed)			
	$\tilde{a}^4A''$ ($m_s = 3/2$)	3.752	3.750	0.05%
	EOM-SF-CCSD/UHF states (response)			
	X^2A' ($m_s = 1/2$)	0.758	0.750	1.13%
	$\tilde{A}^2A''$ ($m_s = 1/2$)	0.753	0.750	0.44%
	$\tilde{B}^2A'$ ($m_s = 1/2$)	0.797	0.750	6.20%
	$\tilde{C}^2A'$ ($m_s = 1/2$)	0.760	0.750	1.36%
	$\tilde{a}^4A''$ ($m_s = 1/2$)	3.756	3.750	0.15%